DOI: 10.1002/((please add manuscript number))
Article type: Communication

Boosting the efficiency of perovskite solar cells with CsBr-modified mesoporous TiO_2 beads as electron selective contact

Ji-Youn Seo[1,], Ryusuke Uchida[2], Hui-seon Kim[3], Yasemin Saygili[3], Jingshan Luo[1], Chris Moore[4], Julie Kerrod[5], Anthony Waggstaff[5], Mike Eklund[5], Robert McIntyre[5], Norman Pellet[1], Shaik M. Zakeeruddin[1], Anders Hagfeldt[3], Michael Grätzel[1,*]*

1 Laboratory of Photonics and Interfaces, Institute of Chemical Sciences and Engineering, École Polytechnique Fédérale de Lausanne (EPFL), Lausanne, CH-1015 Switzerland
2 Advanced Research division, Materials and Devices Research Laboratory, Panasonic Corporation, Kadoma City, Osaka 571-8501, Japan.
3 Laboratory of Photomolecular Science, Institute of Chemical Sciences and Engineering, École Polytechnique Fédérale de Lausanne, CH-1015-Lausanne, Switzerland
4 Dyesol UK, UMIC, Incubator Building, University of Manchester, 48 Grafton St. M13 9XY, United Kingdom
5 Cristal Technology and Innovation Group, La Porte Road, Stallingborough, Grimsby, DN40 2PR, United Kingdom

E-mail: michael.gratzel@epfl.ch; jiyoun.seo@epfl.ch
Keywords: mesoporous TiO_2; perovskite solar cells; Cesium doping; hysteresis; passivation; photovoltaics.

Abstract

Rapid extraction of photo-generated charge carriers is essential to achieve high efficiencies with perovskite solar cells (PSCs). Here we introduce a new mesoscopic architecture as electron selective contact for PSCs featuring 40 nm sized TiO_2 beads endowed with mesopores of a few nm diameter. The bimodal pore distribution inherent to these films produces a very large contact area of 200 m^2/g whose access by the perovskite light absorber is facilitated by the interstitial voids between the particles. Modification of the TiO_2 surface by CsBr further strengthens its interaction with the perovskite. As a result, photo-generated electrons are extracted rapidly producing a very high fill factor of close to 80% a V_{OC} of 1.16 V and a PCE of 21.4% with negligible hysteresis.

There have been numerous studies on perovskite solar cells (PSCs) and solid state dye sensitized solar cells focusing mainly on optimizing methods for film formation and compositional engineering to achieve high power conversion efficiency (PCE) or stability of perovskite solar cells (PSCs), culminating in a certified PCEs of 22.1%.[1–8]

Studies on electron-selective layers (ESLs) have also progressed improving device performance. For example, Sargent et al showed that cesium chloride (CsCl) modification of TiO_2 nanoparticles results in a certified efficiency of 20.1% for a PSC with 0.049 cm^2 active area and enhanced long-term stability in planar perovskite solar cells by defect passivation of the interface between perovskite and the.[9] Another study of TiO_2 modification with metal halides also showed stability and performance improvement of planar PSCs.[10–14] Nevertheless, today's most efficient devices employ still a mesoscopic TiO_2 scaffold as electron selective layer (ESL) despite significant progress on planar PSCs.[2],[9],[15–17]

Although the mesoporous TiO_2 scaffold is considered to be beneficial for PSCs as an electron transport material, there are only few studies of the effect of its architecture and surface modification on the PSC performance. Indeed, mesoscopic perovskite solar cells so far used 30 nm sized TiO_2 nanoparticles that constitute the mesoscopic scaffold acting as ESL lack any porosity their surface being composed of smooth facets with mainly (101) orientation. By contrast there have been several encouraging reports about introducing mesopores in the TiO_2 particles in the area of dye sensitized solar cells (DSSCs) where this resulted in improved device performance.[18],[19] Another issue with TiO_2 is that electron trapping by coordinatively unsaturated Ti (IV) ions is likely to at its interface with the perovskite, which hampers charge transport and enhances radiational charge carrier recombination as well as the appearance of a hysteresis in the J-V curves.[20] Theoretical calculations for TiO_2 suggest that electrons prefer to localize just below the surface being trapped by oxygen vacancies and Ti (IV) ions.[21],[22] One of the most effective methods to reduce the trap states in TiO_2 is surface or bulk doping, which has been widely investigated for mesoporous TiO_2 electrodes in dye-

sensitized solar cells and more recently in PSCs.[23–25] Some dopants reduce the charge recombination and increase electron transport by passivating oxygen defects in the TiO_2 lattice and reducing trap states below the conduction band (CB) of TiO_2 in PSCs. Another effect of doping is the stabilization of power conversion efficiency and the suppression of hysteresis.[25–30]

Here, we test for the first time a 40 nm sized TiO_2 particles being endowed with mesopores to augment the contact area with the perovskite from 60 m^2/g for the conventional scaffold to over 200 m^2/g. In addition we passivate electronically the surface of the mesoporous TiO_2 nano-beads (mp-TiO_2) by treatment with cesium halide (CsX, X = I or Br). We show that this ESL architecture leads to efficient PSCs by enhancement of the contact area and interface passivation between perovskite and mp-TiO_2. We demonstrated that Cs doping induces shift of both oxygen (O) 1s and titanium (Ti) 2p peaks to lower energy, which implies decrease of oxygen vacancy operating as electron trap. As a result, PSCs based on Cs doped mp-TiO_2 and quadruple-cation (Rb/Cs/FA/MA) perovskites exhibit increased electron transport and PCEs up to 21.4% with negligible hysteresis.

At first, we examine the effect of introducing nanopores in the TiO_2 particles that constitute the ESL scaffold. **Figure 1** compares scanning electron microscopy images (SEM) for the conventional films constituted by nonporous particles produced from a commercial paste, 30NR-D (Dyesol) and with the new HTX-100 material (Crystal). The particle size of the latter is larger than that of the standard and the particles are endowed with pores of a few nanometer diameter. These mesoporous beads exhibit a high BET value of 206.31 m^2/g offering a larger contact area to the perovskite than the standard formulation. To investigate effect of surface porosity of TiO_2 on device performance, we made PSCs with same thickness of TiO_2 scaffold layer using non-porous (**Figure 1a**) and the mesoporous beads (**Figure 2b**), respectively. As shown in **Figure S1**, the statics data of photovoltaic parameters shows and improved V_{OC} and

FF with the mesoporous beads. Hence the films made of the mesoporous beads were uses in the studies.

Cs ion doped mp-TiO_2 films were prepared by sintering CsX premixed TiO_2 paste for 30 minutes at 450° C as described in the Experimental Section. Transmission electron microscope (TEM) images of the mp-TiO_2 nanoparticles (NPs) with (CsI, CsBr) and without doping (Control) are shown in **Figure 2**. The TiO_2 nanocrystals are mesoporous with an average size of 40 nm, **Figure 2a**. After treatment with CsX, the morphology of the nanocrystals shows negligible difference compared to the standard TiO_2 scaffold, The Cs ions are well dispersed in the TiO_2 structure, as confirmed by scanning transmission electron microscopy (STEM) coupled with energy-dispersive X-ray spectroscopy (EDX) elemental mapping measurements (**Figure 2c** and **d**), indicating successful and homogenous doping. X-ray photoemission spectroscopy (XPS) was performed to further investigate the elemental composition of the Cs doped and undoped TiO_2. In **Figure 3a**, we observed that the peak of Ti 2p slightly shifted to lower energy from 458.4 eV to 459.0 eV and 457.9 eV by doping with CsI and CsBr, respectively. We also observed O 1s peak shifted to lower energy as shown in **Figure 3b**. The full range of XPS spectra and atomic percent ratio can be found in **Figure S2**. We assumed that Cs more predominantly affected these lower energy shifts than halides because the amount of halide on mp-TiO_2 is very minute compared to Cs. These peak shifts indicate electron transfer to neighbor oxygen vacancies and partial reduction of Ti^{4+} to Ti^{3+} within the TiO_2 lattice. This can passivate the electronic defects or trap states that originate from oxygen vacancies resulting in improved charge transport properties.[27],[31–33] To study the impact of Cs doping on the charge transport within the mp-TiO_2, we prepared dye-sensitized solar cells (DSSCs) using Cs doped mp-TiO_2 as electron transporting layer, as the charge extraction measurement method is well-established to determine the density of state distribution below the TiO_2 conduction band.[34]

In **Figure 3c**, we report the extracted charge curves from the DSSCs at open circuit condition as a function of the open circuit voltage (V_{OC}). At the same V_{OC}, the devices prepared with Cs doped mp-TiO_2 exhibit significantly less charges than the control using mp-TiO_2 without doping because of less density trap state below the CB. This suggests that the Cs doping reduces oxygen vacancies of mp-TiO_2 by partial reduction Ti^{4+} to Ti^{3+}, which helps to passivate the trapping states associated with oxygen vacancies within the TiO_2 lattice. These results show that CsBr is more efficient for doping mp-TiO_2 than CsI.

To further illustrate the effect of Cs doping on perovskite solar cells, first we conducted characterization of perovskite films on the control and CsX doped TiO_2 films. Here, we used quadruple-perovskite ($Rb/Cs/FA_{1-x}/MA_x$) for PSCs developed in our previous study.[15]

In order to investigate the impact of the Cs doped mp-TiO_2 on the morphology and crystal structure of the perovskite film, we collected scanning electron microscopy (SEM) images and X-ray diffraction (XRD) patterns from perovskite films prepared on mp-TiO_2 substrates with and without CsX. In **Figure 4a**, the SEM images show all substrates form perovskite films with pinhole free surface and similar grain size. In **Figure 4b**, we show XRD data. All substrates exhibit the same pattern showing strong typical perovskite peak at 14.2° corresponding to the (110) facet. Full width at half maximum (FWHM) of the (110) peak also shows almost no difference between doped and undoped TiO_2.[35] Therefore, we conclude that CsX doping on mp-TiO_2 does not influence the crystal growth or morphology of the perovskite films.

Steady-state and time-resolved PL spectroscopy were used to study the charge transfer kinetics between perovskite and different ESLs. The steady-state PL was quenched more strongly when the perovskite films was formed on CsX doped mp-TiO_2 (see **Figure 5a**).[36] PL decay curves of perovskite films on the control and CsX doped mp-TiO_2 are shown in **Figure 5b**, the decay lifetime τ is shortened by doping CsI (79.30 ns) and CsBr (49.75 ns) than Control (117.27 ns). The fitting parameters for PL decays are summarized in **Table S1**.

These results indicate faster electron transfer and suppression of interfacial charge recombination at the CsX mp-TiO_2/perovskite interface compared to pristine TiO_2.

To explore the effect of CsX loading of the mesoporous TiO_2 beads on the photovoltaic performance of PSCs, we made devices with the architecture of FTO/cp-TiO_2/mp-TiO_2/Perovskite/spiro-OMeTAD/Au. **Figure S3** presents current density–voltage (*J-V*) curves for the Rb/Cs/$FA_{0.85}$ $MA_{0.15}$ perovskite devices with the pristine mp-TiO_2 (Control), CsI doped mp-TiO_2 (CsI) and CsBr doped mp-TiO_2 (CsBr) (see **Table S2**). The improved open circuit voltage (V_{OC}) and short circuit current (J_{SC}) and fill factor (*FF*) were observed in the devices with Cs doped mp-TiO_2 than undoped one. Hysteresis of devices tends to become smaller using CsBr (4.5%) and CsI (5.2%) compared to control (10.6%). The percentage of hysteresis is determined by 100× {PCE(reverse scan)-PCE(forward scan)}/PCE(reverse scan). Statistics of device performance with Rb/Cs/$FA_{01-x}MA_x$ perovskite on various substrates convince that PSCs are more efficient with CsBr than CsI (See **Figure S4**). As the Cs doping passivated surface traps and reduced recombination in ESLs, the devices produced enhanced performance in PCEs.

To identify the best perovskite composition for CsBr doped mp-TiO_2, we conducted compositional engineering as shown in **Figure 6a**. We tuned the ratio of $MAPbBr_3$ to $FAPbI_3$ from 0 to 0.15. The average of V_{OC} and J_{SC} obtained from 15 devices with CsBr mp-TiO_2 (see **Figure S5**) are plotted in **Figure 6** and it shows tradeoff between V_{OC} and J_{SC}. The best perovskite composition for CsBr doped mp-TiO_2 is achieved when x = 0.05, this is 10% less than our previous best composition on Li-treated mp-TiO_2. With optimized condition, we made devices as shown in **Figure S6** and presented current *J-V* curves of the champion device with the composition Rb/Cs/$FA_{0.95}MA_{0.05}$ under standard AM 1.5G sunlight at 100 mW/cm^2 in **Figure 6b**. The efficiency scanned in forward bias direction was 21.4% with an open-circuit voltage (V_{OC}) of 1.141 V, a short-circuit current density (J_{SC}) of 22.8 mA/cm^2, and a

fill factor (*FF*) of 0.80 with negligible hysteresis (less than 4%). The J_{SC} was confirmed by the integration of the incident photon-to-current efficiency (IPCE) in **Figure S7**.

To pinpoint the added benefit of the CsBr treatment on TiO_2, we performed voltage-dependent IMVS and IMPS measurements.[37] The results were fitted to the reduced model show in **Figure S9** and an example of such fit is shown in **Figure 7**. The IMVS characterization confirmed the added benefit of passivating the TiO_2 surface by cesium by slowing down recombination. This reduced recombination rate directly relates to the increased open circuit voltage observed. We also observed a higher series resistance and a higher charge transfer resistance for the cells treated with CsBr at the same voltage, which resulted in an unchanged collection efficiency around the maximum power point as shown in **Figure S10**, however, the result of collection efficiency also can be interpreted that CsBr dopeTiO_2 help increasing voltage of devices because photocurrents of perovskite show almost same value in **Figure S8** of the devices with and without CsBr treatment in TiO_2.

In order to investigate its long-term shelf-life, we stored the devices with CsBr doped and control mp-TiO_2 under dark and dry air condition for one month (720hours). We confirmed high stability of CsBr devices, the relative value of loss being less then control device after one month storage as shown in **Figure S11**.

In conclusion, we examined the shape effect of TiO_2 on device performance and Cs doping on the mesoscopic TiO_2 as an ESL in PSCs by simple fabrication method same as normal mp-TiO_2. The cesium induces a partial reduction of Ti^{4+} and passivates electron trap states in TiO_2 lattice. The presence of Cs on the mp-TiO_2 improves electron transfer and reduces recombination at the perovskite/ESLs interface in PSCs. Remarkably by using optimized cation mixture of Rb/Cs/$FA_{0.95}MA_{0.05}$ perovskite, we achieved a PCE of 21.4% with negligible hysteresis.

Experimental Section

Substrate preparation and Cs-doping TiO_2 Nippon Sheet Glass 10 Ω/sq was cleaned by sonication in 2% Hellmanex water solution for 30 minutes. After rinsing with deionised water and ethanol, the substrates were further cleaned with UV ozone treatment for 15 min. Then, 30 nm TiO_2 compact layer was deposited on FTO via spray pyrolysis at 450°C from a precursor solution of titanium diisopropoxide bis(acetylacetonate) in anhydrous ethanol. After the spraying, the substrates were kept at 450°C for 45 min and left to cool down to room temperature. TiO_2 pastes was used 30 NR-D (Dyesol) and HTX-100 (Crystal). 5wt% of CsX (X= I and Br) premixed mp-TiO_2 paste was obtained from Crystal (HTX100i and HPX100b Product code) for mp-TiO_2 layer. mp-TiO_2 layer was deposited by spin coating for 20 s at 4000 rpm with a ramp of 2000 rpm per second to achieve a 150-200 nm thick layer. After the spin coating, the substrates were immediately dried at 100°C for 10 min and then sintered again at 450°C for 30 min under dry air flow. After cooling down to 150°C the substrates were immediately transferred in a nitrogen atmosphere glove box for depositing the perovskite films.

Perovskite precursor solution and film preparation The organic cations were purchased from Dyesol; the lead compounds from TCI; CsI from abcr GmbH. The perovskite precursor were dissolved in anhydrous DMF:DMSO 4:1 (v:v). We note that 10% excess PbI_2 and $PbBr_2$ are used for perovskite precursor solution. The Rb/Cs/$FA_{1-x}MA_x$ perovskite precursor solutions were deposited from a precursor solution containing FAI 1.2*(1-x) M, PbI_2 1.3*(1-x) M, MABr 1.2*x M and $PbBr_2$ 1.3*x M in anhydrous DMF:DMSO 4:1 (v:v) (x= 0, 0.05, 0.15). Then CsI, predissolved as a 1.5 M stock solution in DMSO, was added to the mixed perovskite (FA/MA) precursor to make Cs/FA/MA triple cation perovskite. RbI was also predissolved as a 1.5 M stock solution in DMF:DMSO 4:1 (v:v) and then was added to the Cs/FA/MA triple cation perovskite to achieve the desired quadruple composition. The

perovskite solution was spin coated in a two steps program at 1000 and 4000 rpm for 10 and 20 s respectively. During the second step, 200 µL of chlorobenzene was poured on the spinning substrate 15 s prior to the end of the program. The substrates were then annealed at 100°C for 30min in a nitrogen filled glove box (only for the device with annealed perovskite).

Hole transporting layer and top electrode After the perovskite annealing, the substrates were cooled down for few minutes and a spiro-OMeTAD (Merck) solution (70 mM in chlorobenzene) was spin coated at 4000 rpm for 20 s. Spiro-OMeTAD was doped with bis(trifluoromethylsulfonyl)imide lithium salt (Li-TFSI, Sigma-Aldrich), tris(2-(1H-pyrazol-1-yl)-4-tert-butylpyridine)-cobalt(III) tris(bis(trifluoromethylsulfonyl)imide) (FK209, Dynamo) and 4-tert-Butylpyridine (TBP, Sigma-Aldrich). The molar ratio of additives for spiro-OMeTAD was: 0.5, 0.03 and 3.3 for Li-TFSI, FK209 and TBP respectively. Finally, 70-80 nm of gold top electrode was thermally evaporated under high vacuum.

DSSC preparation procedure In order to prepare DSC devices, firstly FTO substrates (NSG-10, Nippon Sheet Glass) were pre-treated with a detergent solution (Deconex) in ultrasonic bath and UV/O_3 (Model no.256-220, Jelight Company, Inc.), respectively. A TiO2 underlayer is prepared by immersing the substrates in 40mM $TiCl_4$ solution at 70ºC for 30 minutes. The pastes were screen printed (≈ 3 µm) on the substrates prior to sintering process. The Working electrodes were dipped for 16 hours in 0.1mM of Y123 dye solution (Dyenamo AB). For counter electrodes, FTO glass (TEC 6, Pilkington) were coated with PEDOT via electrodeposition[38],[39] 25µm Surlyn spacer (Dupont) used for assembling the working electrode and counter electrodes and electrolyte encapsulation. The electrolytes prepared with 0.2 M Cu(I)tmby and 0.04 M Cu(II)tmby complexes, 0.1M LiTFSI and 0.6 M TBP in acetonitrile. A detailed device preparation description can be found in the publication of Saygili et al.[38]

Charge extraction techniques Charge extraction and electron transport times in DSC devices as a function of open-circuit voltages were measured via DYENAMO Toolbox System. The system mainly consists of a white LED light source (Seoul Semiconductors), a 16-bit resolution digital acquisition board (National Instruments) in order to record voltage traces and a current amplifier (Thorlabs PDA200C). For charge extraction, firstly, the DSCs were kept at open-circuit conditions and then they were illuminated by the light source. After 1 second the light was turned off and the device was switched to short-circuit condition. The total charge was obtained through the integration of current with respect to time. The complete charge-potential curve was obtained by using different light intensities

Photovoltaic device testing The solar cells were measured using a 450 W xenon light source (Oriel). The spectral mismatch between AM1.5G and the simulated illumination was reduced by the use of a Schott K113 Tempax filter (Präzisions Glas & Optik GmbH). The light intensity was calibrated with a Si photodiode equipped with an IR-cutoff filter (KG3, Schott), and it was recorded during each measurement. Current-voltage characteristics of the cells were obtained by applying an external voltage bias while measuring the current response with a digital source meter (Keithley 2400). The voltage scan rate was 10 mV s^{-1} and no device preconditioning, such as light soaking or forward voltage bias applied for long time, was applied before starting the measurement. The starting voltage was determined as the potential at which the cells furnish 1 mA in forward bias, no equilibration time was used. The cells were masked with a black metal mask (0.16 cm^2) to fix the active area and reduce the influence of the scattered light. The current was matched according to the intensity of the light source. Incident photon to current efficiency (IPCE) spectra were recorded using the Ariadne

system (Cicci Research). A non-reflective metallic mask with an aperture of 0.16 cm^2 was used during both measurements.

Perovskite characterization A ZEISS Merlin HR-SEM was used to characterize the morphology of the device top view and cross-section. TiO_2 particles were characterized by a high-resolution transmission electron microscope (Technai Osiris, FEI). The composition of TiO_2 nanoparticles were characterized by the energy-dispersive X-ray (EDX) spectra obtained in scanning transmission electron microscopy (STEM) mode with Technai Osiris. X-Ray Photoelectron Spectroscopy (XPS) measurements were carried out using a PHI VersaProbe II scanning XPS microprobe (Physical Instruments AG, Germany). X-ray diffraction (XRD) were recorded on an Empyrean (Panalytical) equipped with a ceramic tube (Cu anode, λ = 1.54060 Å), Reflection-Transmission Spinner, a PIXcel^{1D} (Panalytical) in an angle range of 2θ = 5° to 60° under ambient condition. Absorption spectral measurements were recorded using Varian Cary5 UV–visible spectrophotometer. Photoluminescence spectra were obtained with Florolog 322 (Horiba Jobin Ybon Ltd) with the range of wavelength from 620 to 850nm by exciting at 460nm. The samples were mounted at 60° and the emission recorded at 90° from the incident beam path. The time-resolved photoluminescence (TRPL) is incorporated into the same Fluorolog-312 spectrofluorometer. The exciting source is now a NANOLed 408 nm pulsed diode laser with a pulse width of less than 200 ps and repetition rate of 1 MHz.

The IMVS and IMPS measurements IMPS IMVS and IMPS spectra were recorded as a function of voltage using a home-made instrumentation. The modulated light source consisted of Coherent OBIS 422 CW laser diode. The light beam was split into two components (Thorlabs EBP1). The first component was directed into a 50-Ohm loaded biased silicon reference diode (Thorlabs DET10A). The second component was directed onto a beam

diffuser (Thorlabs DG220) behind which the sample was placed (~2cm away from the diffuser). A DC light bias was provided by additional blue LEDs, such that the total illumination intensity reached about 10 mW/cm^2. The device was connected to a home-made preamplifier that enforces galvanostatic or potentiostatic conditions and provide an amplified signal for the frequency response analyzer (FRA). The FRA (Metrohm Autolab FRA2) v-channel was connected to the analog remote of the laser diode, the x-channel was connected to the reference diode and the y-channel to the preamplifier. All measurements were recorded as a function of voltage and both IMPS and IMVS spectra were fitted together using a Levenberg-Marquart non-linear least square fitting algorithm (Igor Pro 6.3). For each iteration of the fitting loop, the solution of the model shown in **Figure S12** was generated using an AC solver (SPICE), which input parameters were provided by the fitting loop. The collection efficiency was calculated based on the transport and recombination resistance, excluding the charge transfer resistance. We note that this interpretation remains valid even if interfacial recombination were the leading loss pathway.

Supporting Information
Supporting Information is available from the Wiley Online Library or from the author.

Acknowledgements
MG thanks the financial support from the Swiss National Science Foundation, the SNSF-NanoTera (SYNERGY) and Swiss Federal Office of Energy (SYNERGY), CCEM-CH in the 9th call proposal 906: CONNECT PV, the SNSF NRP70 "Energy Turnaroun and the European Union's Horizon 2020 research and innovation programme under the grant agreement No 687008 is gratefully acknowledged. The information and views set out in this article are those of the author(s) and do not necessarily reflect the official opinion of the European Union.

Received: ((will be filled in by the editorial staff))
Revised: ((will be filled in by the editorial staff))
Published online: ((will be filled in by the editorial staff))

[1] B. Li, L. Wang, B. Kang, P. Wang and Y. Qiu, *Sol. Energy Mater. Sol. Cells*, 2006, 90, 549–573.

[2] D. Bi, W. Tress, M. I. Dar, P. Gao, J. Luo, C. Renevier, K. Schenk, A. Abate, F. Giordano, J.-P. Correa Baena, J.-D. Decoppet, S. M. Zakeeruddin, M. K. Nazeeruddin, M. Gra tzel and A. Hagfeldt, *Sci. Adv.*, 2016, **2**, e1501170–e1501170.

[3] N. J. Jeon, J. H. Noh, Y. C. Kim, W. S. Yang, S. Ryu and S. Il Seok, *Nat Mater*, 2014, **13**, 897–903.

[4] M. M. T. Lee J Miyasaka, T Murakami, TN Snaith, HJ, *Sci.*, 2012, **338**, 647.

[5] A. Kojima, K. Teshima, Y. Shirai and T. Miyasaka, *J. Am. Chem. Soc.*, 2009, **131**, 6050–6051.

[6] N. J. Jeon, J. H. Noh, W. S. Yang, Y. C. Kim, S. Ryu, J. Seo and S. Il Seok, *Nature*, 2015, **517**, 476–480.

[7] National Renewable Energy Laboratory(NREL), BestResearch-Cell Efficiencies. Available at: https://www.nrel.gov/pv/assets/images/efficiency-chart.png.

[8] H.-S. Kim, C.-R. Lee, J.-H. Im, K.-B. Lee, T. Moehl, A. Marchioro, S.-J. Moon, R. Humphry-Baker, J.-H. Yum, J. E. Moser, M. Grätzel and N.-G. Park, *Sci. Rep.*, 2012, **2**, 591.

[9] H. Tan, A. Jain, O. Voznyy, X. Lan, F. P. García de Arquer, J. Z. Fan, R. Quintero-Bermudez, M. Yuan, B. Zhang, Y. Zhao, F. Fan, P. Li, L. N. Quan, Y. Zhao, Z.-H. Lu, Z. Yang, S. Hoogland and E. H. Sargent, *Sci.*, 2017, **355**, 722–726.

[10] L. Qin, Z. Xie, L. Yao, Y. Yan, S. Pang, F. Wei and G. G. Qin, *Phys. Status Solidi - Rapid Res. Lett.*, 2014, **8**, 912–916.

[11] H. Zhang, J. Shi, X. Xu, L. Zhu, Y. Luo, D. Li and Q. Meng, *J. Mater. Chem. A*, 2016, **4**, 15383–15389.

[12] D. Liu, S. Li, P. Zhang, Y. Wang, R. Zhang, H. Sarvari, F. Wang, J. Wu, Z. Wang and Z. D. Chen, *Nano Energy*, 2017, **31**, 462–468.

[13] X. Zhang, Z. Bao, X. Tao, H. Sun, W. Chen and X. Zhou, *RSC Adv.*, 2014, **4**, 64001–64005.

[14] W. Li, J. Li, G. Niu and L. Wang, *J. Mater. Chem. A*, 2016, **4**, 11688–11695.

[15] M. Saliba, T. Matsui, K. Domanski, J.-Y. Seo, A. Ummadisingu, S. M. Zakeeruddin, J.-P. Correa-Baena, W. R. Tress, A. Abate, A. Hagfeldt and M. Gratzel, *Sci.*, 2016, **354**, 206.

[16] X. Li, D. Bi, C. Yi, J.-D. Décoppet, J. Luo, S. M. Zakeeruddin, A. Hagfeldt and M. Grätzel, *Science*, 2016, **353**, 58–62.

[17] S. S. Shin, E. J. Yeom, W. S. Yang, S. Hur, M. G. Kim, J. Im and J. Seo, *Sci.*, , DOI:10.1126/science.aam6620.

[18] A. Tricoli, A. S. Wallerand and M. Righettoni, *J. Mater. Chem.*, 2012, **22**, 14254.

[19] D. Chen, F. Huang, Y. B. Cheng and R. A. Caruso, *Adv. Mater.*, 2009, **21**, 2206–2210.

[20] C. Di Valentin and A. Selloni, *J. Phys. Chem. Lett.*, 2011, **2**, 2223–2228.

[21] Y. F. Ji, B. Wang and Y. Luo, *J. Phys. Chem. C*, 2012, **116**, 7863–7866.

[22] N. A. Deskins, R. Rousseau and M. Dupuis, *J. Phys. Chem. C*, 2009, **113**, 14583–14586.

[23] F. Giordano, A. Abate, J. Pablo, C. Baena, M. Saliba, T. Matsui, S. H. Im, S. M. Zakeeruddin, M. K. Nazeeruddin, A. Hagfeldt and M. Graetzel, *Nat. Commun.*, 2016, **7**, 1–6.

[24] M. Kitahara, Y. Shimasaki, T. Matsuno, Y. Kuroda, A. Shimojima, H. Wada and K. Kuroda, *Chem. - A Eur. J.*, 2015, **21**, 13073–13079.

[25] B. Roose, S. Pathak and U. Steiner, *Chem. Soc. Rev.*, 2015, **44**, 8326–8349.

[26] H. Zhou, Q. Chen, G. Li, S. Luo, T. -b. Song, H.-S. Duan, Z. Hong, J. You, Y. Liu and Y. Yang, *Sci.*, 2014, **345**, 542–546.

[27] U. B. Cappel, A. L. Smeigh, S. Plogmaker, E. M. J. Johansson, H. Rensmo, L. Hammarström, A. Hagfeldt and G. Boschloo, *J. Phys. Chem. C*, 2011, **115**, 4345–4358.

[28] A. K. Chandiran, F. Sauvage, M. Casas-Cabanas, P. Comte, S. M. Zakeeruddin and M. Graetzel, *J. Phys. Chem. C*, 2010, **114**, 15849–15856.

[29] F. Huang, Y. B. Cheng and R. A. Caruso, *Aust. J. Chem.*, 2011, **64**, 820–824.

[30] M. Wang, S. Bai, A. Chen, Y. Duan, Q. Liu, D. Li and Y. Lin, *Electrochim. Acta*, 2012, **77**, 54–59.

[31] M. A. Henderson, W. S. Epling, C. H. F. Peden and C. L. Perkins, *J. Phys. Chem. B*, 2003, **107**, 534–545.

[32] C. L. Olson, J. Nelson and M. S. Islam, *J. Phys. Chem. B*, 2006, **110**, 9995–10001.

[33] A. Abate, T. Leijtens, S. Pathak, J. Teuscher, R. Avolio, M. E. Errico, J. Kirkpatrik, J. M. Ball, P. Docampo, I. McPherson and H. J. Snaith, *Phys. Chem. Chem. Phys.*, 2013, **15**, 2572–2579.

[34] P. R. F. Barnes, K. Miettunen, X. Li, A. Y. Anderson, T. Bessho, M. Gratzel and B. C. O'Regan, *Adv. Mater.*, 2013, 25, 1881–1922.

[35] J. Burschka, N. Pellet, S.-J. Moon, R. Humphry-Baker, P. Gao, M. K. Nazeeruddin and M. Grätzel, *Nature*, 2013, **499**, 316–320. 1

[36] Y. H. Lee, J. Luo, M. K. Son, P. Gao, K. T. Cho, J. Seo, S. M. Zakeeruddin, M. Grätzel and M. K. Nazeeruddin, *Adv. Mater.*, 2016, **28**, 3966–3972.

[37] P. Norman, PhD thesis, 2017, Polytechnique Federale de Lausanne.

[38] H. Ellis, N. Vlachopoulos, L. Häggman, C. Perruchot, M. Jouini, G. Boschloo and A. Hagfeldt, *Electrochim. Acta*, 2013, **107**, 45–51.

[39] Y. Saygili, M. Söderberg, N. Pellet, F. Giordano, Y. Cao, A. B. Munoz-García, S. M. Zakeeruddin, N. Vlachopoulos, M. Pavone, G. Boschloo, L. Kavan, J. E. Moser, M. Grätzel, A. Hagfeldt and M. Freitag, *J. Am. Chem. Soc.*, 2016, **138**, 15087–15096.

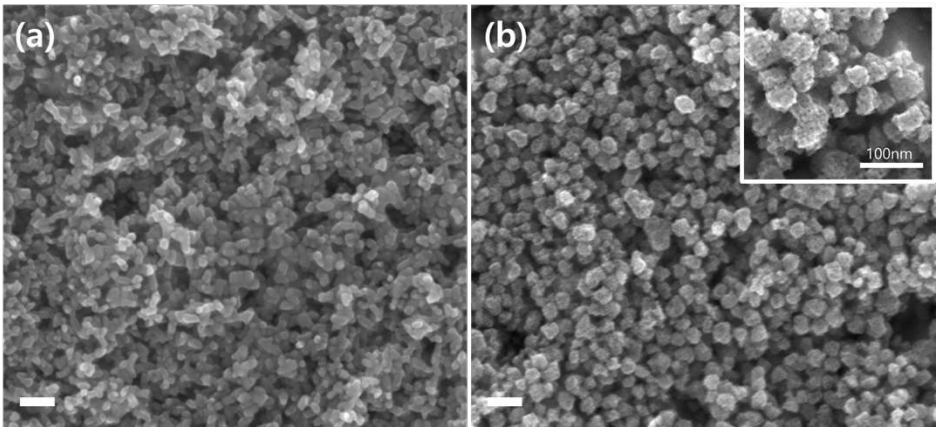

Figure 1. SEM images of the mesoporous TiO_2 particles. (a) 30NR-D and (b) HTX-100, respectively. Scale bar is 100 nm.

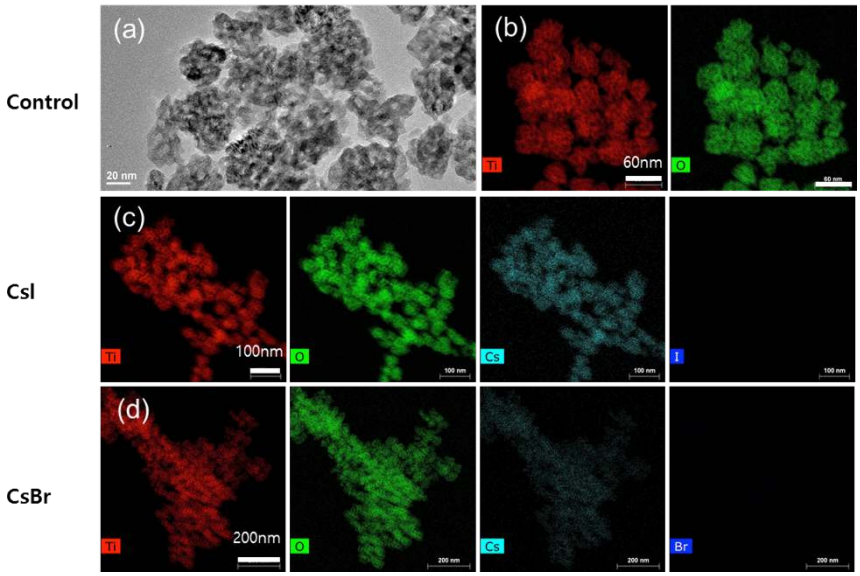

Figure 2. TEM and EDX elemental mapping characterizations of the mesoporous TiO_2 particles. (a) High-resolution TEM image and element mapping of (b) Ti and O for Control and (c-d) element mapping of Ti, O, Cs and I for a CsI and CsBr doped TiO_2 particles, respectively.

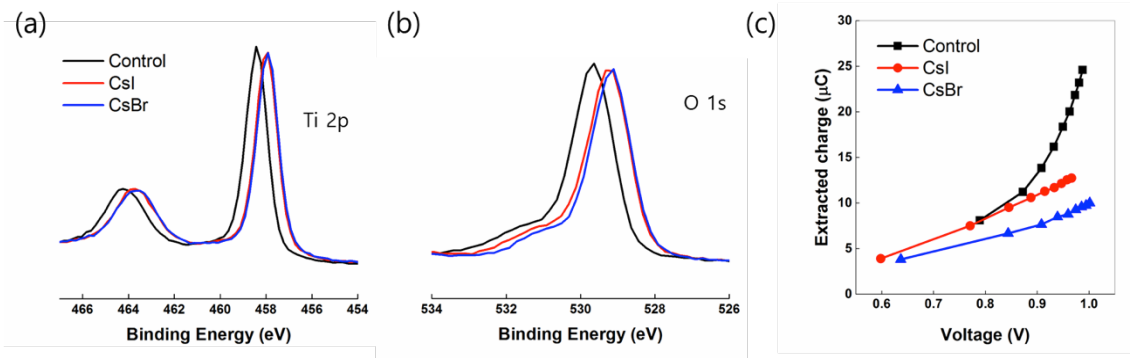

Figure 3. X-ray photoelectron spectroscopy spectra of mesoporous TiO_2 layers. (a) Ti 2p peaks and (b) O 1s peaks of non-doped sample (black), CsI doped sample (red) and CsBr doped sample (blue) respectively. (c) Charge extracted at open circuit as function of the voltage for dye-sensitized solar cells prepared without and with Cs-doped mesoporous TiO_2.

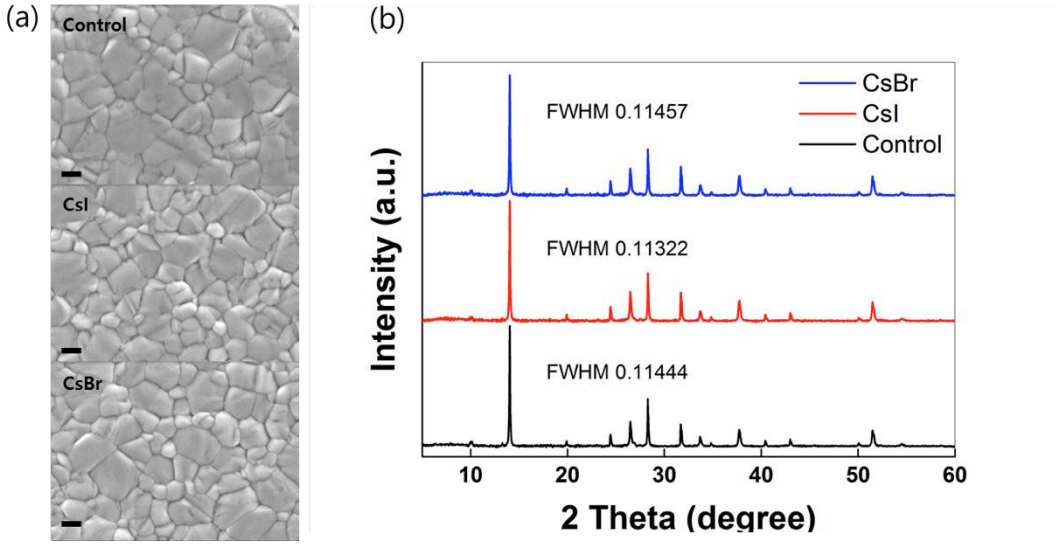

Figure 4. Morphological analysis of perovskite films with and without CsX (X = I and Br). (a) Top-view SEM images and (b)X-ray diffraction diagram (XRD) of perovskite films deposited on various mp-TiO_2/cp-TiO_2/FTO substrates annealed at 100°C for 1hr, the intensity of XRD is normalized to the peak at 14° (110) and FWHM is calculated from (110) peak.

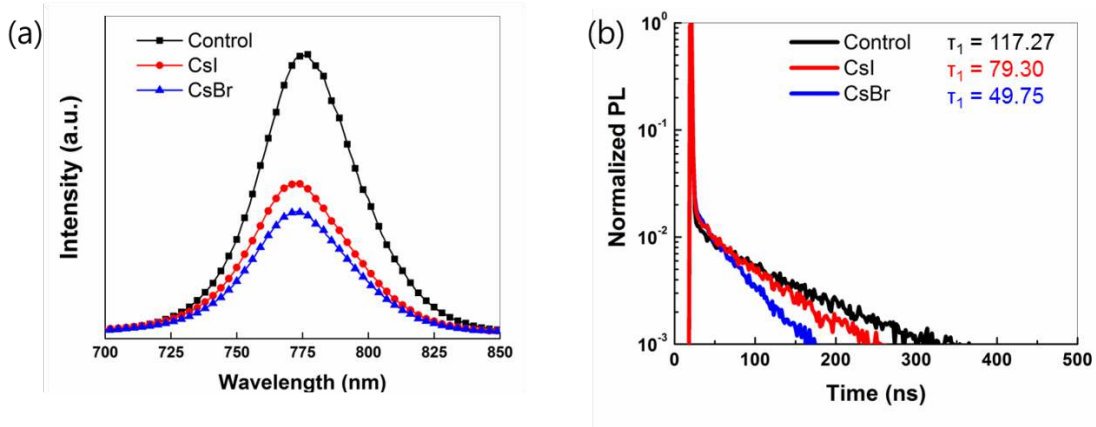

Figure 5. Photoluminescence characterization. (a)Steady-state photoluminescence (PL) emission spectra and (b) Normalized time-resolved photoluminescence (TRPL) decay plots of the perovskite films on various substrates with and without CsX doping (X=I and Br)

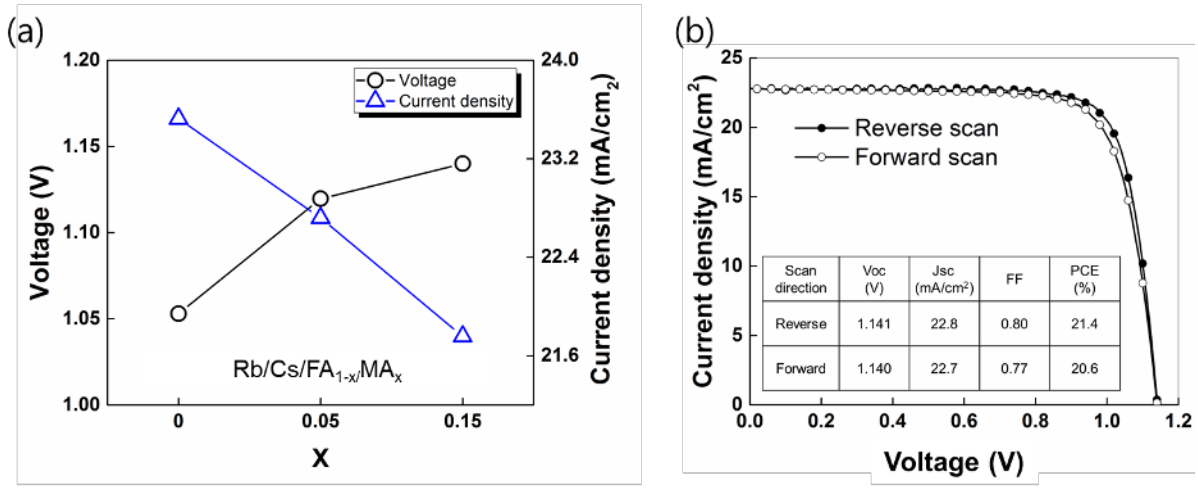

Figure 6. Photovoltaic performance of PSCs. (a) Compositional engineering to optimize the $MAPbBr_3/FAPbI_3$ ratio effect on the open circuit voltage and current density and (b) Current density–voltage (*J-V*) curves of the champion device prepared with CsBr doped mp-TiO_2. The *J-V* curves were taken at 10 mV/s scan rate under AM1.5 simulated solar light. The inset shows the photovoltaic parameters collected from *J-V* curves (PCE, reverse and forward scan). The device active area was defined using a black metal shadow mask with an aperture of 0.16 cm^2.

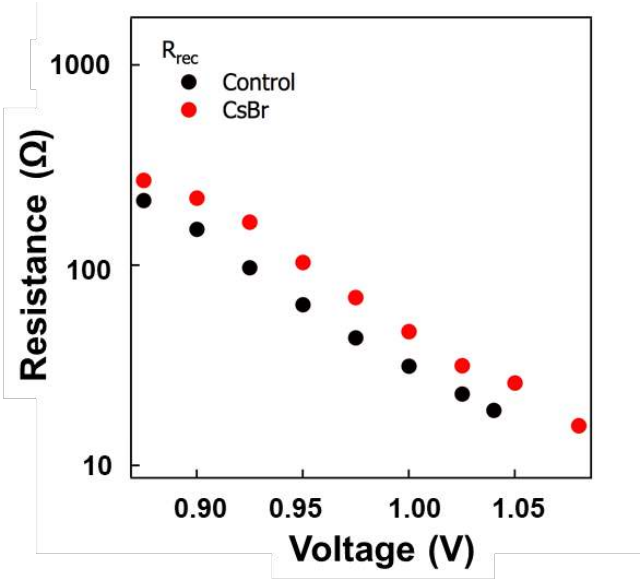

Figure 7. IMVS and IMPS measurements. Recombination resistance (R_{rec}) of the control device (black circles) and the optimized device with CsBr doped mp-TiO_2 (red circles).

Cesium modification of bimodal mesoporous TiO_2 surface for perovskite solar cells (PSCs) enhanced a power conversion efficiency (PCE) of 21.4%. The presence of Cs on the mp-TiO_2 improves electron transfer and reduces recombination at the interface between perovskite and elective selective layers in PSCs. As a result, photo-generated electrons are extracted rapidly producing a very high fill factor of close to 80% a V_{OC} of 1.16 V and a PCE of 21.4% with negligible hysteresis.

Keyword mesoporous TiO_2; perovskite solar cells; Cesium doping; hysteresis; passivation; photovoltaics.

Ji-Youn Seo[1,], Ryusuke Uchida[2], Hui-seon Kim[3], Yasemin Saygili[3], Jingshan Luo[1], Chris Moore[4], Julie Kerrod[5], Anthony Waggstaff[5], Mike Eklund[5], Robert McIntyre[5], Norman Pellet[1], Shaik M. Zakeeruddin[1], Anders Hagfeldt[3], Michael Grätzel[1,*]*

Boosting the efficiency of perovskite solar cells with CsBr-modified mesoporous TiO_2 beads as electron selective contact